Icarus 355 (2021) 114179

Contents lists available at ScienceDirect

Icarus

journal homepage: www.elsevier.com/locate/icarus

Exospheric Na distributions along the Mercury orbit with the THEMIS telescope

Anna Milillo [a,*], Valeria Mangano [a], Stefano Massetti [a], Alessandro Mura [a], Christina Plainaki [b], Tommaso Alberti [a], Alessandro Ippolito [b], Stavro L. Ivanovski [c], Alessandro Aronica [a], Elisabetta De Angelis [a], Adrian Kazakov [a], Raffaella Noschese [a], Stefano Orsini [a], Rosanna Rispoli [a], Roberto Sordini [a], Nello Vertolli [a]

[a] INAF/IAPS, Italy
[b] ASI, Italy
[c] INAF/OATs, Italy

A B S T R A C T

The Na exosphere of Mercury is characterized by the variability of the emission lines intensity and of its distribution in time scales from less than one hour to seasonal variations. While the faster variations, accounting for about 10–20% of fluctuations are probably linked to the planetary response to solar wind and Interplanetary Magnetic Field variability, the seasonal variations (up to about 80%) should be explained by complex mechanisms involving different surface release processes, loss, source and migrations of the exospheric Na atoms. Eventually, a Na annual cycle can be identified. In the past, ground-based observations and equatorial density from MESSENGER data have been analyzed. In this study, for a more extensive investigation of the exospheric Na features, we have studied the local time and latitudinal distributions of the exospheric Na column density as a function of the True Anomaly Angle (TAA) of Mercury by means of the extended dataset of images, collected from 2009 to 2013, by the THEMIS solar telescope. Our results show that the THEMIS images, in agreement with previous results, registered a strong general increase in sodium abundance at aphelion and a dawn ward emission predominance with respect to dusk ward and subsolar region between 90° and 150° TAA. This behavior can be explained by desorption of a sodium surface reservoir consisting of sodium that is pushed anti-sunward and condenses preferentially in the coldest regions. Our analyses shows a predominance of subsolar line-of-sight column density along the rest of Mercury's orbit. An unexpected relationship between Northward or Southward peak emission and both TAA and local time is also shown by our analysis. This result seems to contradict previous results obtained from different data sets and it is not easily explained, thus it requires further investigations.

1. Introduction

The Sodium exosphere of Mercury is a useful means for the investigation of the active processes and mechanisms in the Mercury – interplanetary medium interactions; in fact, the Na atoms, being volatile, are released from the Mercury's surface mainly by the effect of solar thermal radiation, photons, and solar wind as well as micrometeoroids impacts (e.g.: Killen and Ip, 1999; Milillo et al., 2010; Raines et al., 2015; Milillo et al., 2020).

Mercury's Na exosphere observations have been obtained by ground based observations with many telescopes and by space observations by MESSENGER (Solomon et al., 2007). The ground based observations often show a double peak at mid-high latitudes with time scale variations less than one hour unrelated to any surface feature (e.g.: Potter and Morgan, 1985; Potter et al., 2006; Leblanc et al., 2009; Mangano et al., 2015; Massetti et al., 2017), while the MESSENGER/MASCS UVVS (McClintock and Lankton, 2007) observations have a strong seasonal dependence and show little evidence of a short time-scale variability (e.g.: Cassidy et al., 2015, 2016). This discrepancy may be due to the fact that the MESSENGER/MASCS measurements published by Cassidy et al. (2015) mainly describe the dayside equatorial distribution, since these data were mostly taken from the southern MESSENGER apocenter looking above, when the viewing geometry allowed to image only the limb exosphere near the equatorial region. Hence, from this MASCS data set it was not possible to catch the mid latitudes variations (Cassidy et al., 2015), as fully observed from the Earth for nearly four decades.

The science community is divided between those convinced that the two variable peaks are linked to solar wind precipitation and that Sun's activity is **a** major driver of the Na exosphere configuration at Mercury (e.g.: Killen et al., 2001; Mura et al., 2009; Mangano et al., 2013; Orsini et al., 2018), and those convinced that the Na variability is only related to the surface temperatures variations on long time scales or to the

* Corresponding author.
E-mail address: anna.milillo@inaf.it (A. Milillo).

https://doi.org/10.1016/j.icarus.2020.114179
Received 6 April 2020; Received in revised form 17 September 2020; Accepted 20 October 2020
Available online 24 October 2020

position along the orbit linked to different effect of radiation pressure (e.g.: Potter et al., 2007; Leblanc and Johnson, 2010; Cassidy et al., 2016) or due to the crossing of the interplanetary dust disk (Kameda et al., 2009). Killen and Hahn (2015) conducted an extensive study on the effect of the interplanetary dust disk and of meteoroid stream on the Ca exosphere, showing a steep increase at TAA about 30° when the comet Encke/2P stream intersects Mercury's orbit. In principle, the dust could produce a similar effect on the Na exosphere. Often, a clear distinction between these scenarios cannot be attained (e.g.: Milillo et al., 2020) and the real situation may be the result of a combination of the aforementioned mechanisms.

Nevertheless, different time-scale variations are due to different mechanisms. While short time scales, accounting for 10–20% of the overall variability (Potter et al., 1999; Mangano et al., 2013; Massetti et al., 2017; Orsini et al., 2018), and double peak distributions can be linked to solar wind impact onto the surface along the magnetic field lines, the larger variations of the total Na content of the exosphere along the Mercury orbit are not easily linked to solar wind- magnetosphere interaction.

When dealing with the average Na emission (unit kilorayleigh, kR), it must be taken into account that most of the observed annual variability is due to the variation of the rate at which Na scatters solar photons (unit photons/(atoms s)), that is, the *g*-factor, (Leblanc and Johnson, 2010). Given Na absorption efficiency in the solar spectrum, Na *g* factor is highly variable along the Mercury's eccentric orbit due to the distance variation from the Sun and to the Doppler shift, i.e. the radial velocity (Killen et al., 2009). Therefore, for a quantitative analysis of the Na exosphere variability the observations must be converted to column densities (unit atoms/cm^2) (Leblanc et al., 2008; Cassidy et al., 2015).

Potter et al. (2007) noted that during there is a general decrease in Na normalized emission efficiency when Mercury moves toward the Sun (inbound leg), while it increases when Mercury moves out from the Sun (outbound leg). Na exospheric atoms accelerate due to radiation pressure with positive feedback while Mercury moves anti-sunward, and negative feedback when moving sunward, as explained in their paper.

The subsolar Na exospheric density has been derived by the MASCS observations along the Mercury's year, revealing a decrease from perihelion to TAA 90° and from aphelion toward TAA 270°, in contrast the subsolar density strongly increases while approaching aphelion (Cassidy et al., 2015). These seasonal variabilities seem quite predominant with respect to the variabilities described by Potter et al. (2007), and the trend was explained as the combined effect of radiation pressure that accelerates the Na atoms mainly in the mid seasons (TAA 45°–135° and 125°–305°) and photoionization rate that is lower at aphelion, both effects minimizing the loss rate at aphelion phase.

Leblanc and Johnson (2010) suggested that different processes are dominant along the Mercury's orbit, more specifically, thermal desorption (TD) during the retrograde phase (TAA >330° and <25°) and photon stimulated desorption (PSD) during 25° < TAA < 330°.

A dawn-side enhancement with respect to the dusk-side was observed and considered statistically relevant by different Earth-based observations (Sprague et al., 1997; Schleicher et al., 2004; Potter et al., 2006). The Na atoms are considered to fall back to the surface and condense in the cold night side remaining there until these regions are brought under sunlight (Leblanc and Johnson, 2003, 2010; Mura et al., 2009). The MASCS data (Cassidy et al., 2016) showed that the Na column density is generally higher above the so-called "cold-pole", that is, the geographic region on the Mercury's surface at lowest average temperature. More specifically, when the cold-pole is in the dawn side (approaching the aphelion) the dawn-side emission is much higher than the dusk-side one. In contrast, the dusk-side emission is higher than the dawn-side while moving away from aphelion. But this asymmetry is observed to be less significant since the maximum densities at dusk in post aphelion are about half of those at dawn at pre aphelion.

Kameda et al. (2009), by analyzing the full disk column densities of the Potter et al. (2006) dataset, found that they are anticorrelated with the distance from the ecliptic plane. In fact, Mercury's orbit extends out of the ecliptic plane where the dust disk is mostly located. Hence, they concluded that the Na exosphere is mostly generated through micrometeoroid impact vaporization, although such a scenario cannot explain the double-peak distribution.

Based on a statistical study of ground-based (e.g., Na-exosphere distributions) and space-based (e.g., Interplanetary Magnetic Field (IMF) components), Mangano et al. (2015) related the occurrence of different features in Mercury's exosphere (e.g., double peak, northern, equatorial or southern emission) to the IMF configuration. These authors showed that the double peak pattern is the most common (60%) and that the Northern emission is usually predominant during the East elongation (duskward hemisphere view), while the southern peak emission seems to be related to the Western elongation (dawnward hemisphere view). This asymmetry has, at the moment, no explanation. However, the authors also found that when near full disk of Mercury was on view the two peaks appeared to be closely aligned in longitude, suggesting that the dawn/dusk asymmetry should not be associated with an observational bias due to a prenoon/postnoon displacement of the two (northern and southern) emission spots but they are linked to precipitation of solar wind toward the two sub cusp regions along similar field lines.

In this study, we want to investigate the long-term variability and asymmetries of the Na exospheric distributions along the Mercury's orbit by using the same THEMIS data set of Mangano et al. (2015), as described in Section 2. In Section 3, the data analysis is described. As a first analysis, we investigate the latitudinal variation along the Mercury's orbit, including northern versus southern peak behavior. Then we investigate possible local time asymmetries only in the equatorial region and compare the results with previously published studies derived from MESSENGER/MASCS and other ground-based data sets.

In Section 4, we discuss the results, summary and conclusions in view of the upcoming BepiColombo measurements, are given in Section 5.

2. Data set

Earth-based data are obtained by using the THEMIS solar telescope López-Ariste et al. (2000) located in Tenerife (Canaries, Spain). THEMIS telescope has a 0.9 m primary mirror and a 15.04 m focal length and it can be used during the daylight to image Mercury Na exosphere above the disk for several hours per day.

Since 2009, THEMIS was used together with the MulTiRaies spectrometer in multiline mode (Mein and Rayrole, 1985), with two different cameras observing both the Na D1 (589.6 nm) and D2 (589.1 nm) lines at the same time. Notable results have been obtained thanks to this wide database (available at http://themis.iaps.inaf.it) and thanks to its high spatial and spectral resolution (Leblanc et al., 2008, 2009, 2013; Leblanc and Johnson, 2010; Mangano et al., 2013, 2015; Massetti et al., 2017; Orsini et al., 2018).

The spectral dispersion was 11 mÅ per pixel and the spectral resolution 27mÅ, about 220,000 resolving power. For further details on the observational setup and procedure refer to the papers cited above.

In the present paper, we used the D2 emission measurements achieved along five consecutive years, between 2009 and 2013 (see Table 1). We limit the present analysis to periods of seeing conditions $\sigma \leq 3''$. These data cover almost all the Mercury's seasons.

Some examples of observed images are shown in Fig. 1 and a summary of the observation periods including information on the most significant related parameters is given in Table 1.

3. Data analysis

3.1. Colum density

To convert the observed Na D2 intensity into column density we need to divide it for the *g*-factor (*g*) that is the rate (s^{-1}) at which a sodium atom scatters solar photons in this line. It depends on the distance from

Table 1
THEMIS observation campaigns: periods, ranges of TAA, Phase Angle (PA), radial component of Mercury's velocity, derived g-factor.

Period	TAA [°]	PA [°]	Radial velocity [km/s]	g-factor [phot./(atoms s)]
Apr 2009	37–75	69–97	+6.2 to +9.6	27–38
Jun 2009	280–317	−75 to −51	−9.9 to −7.0	34–38
Oct 2009	74–106	−40 to −17	+9.4 to +10.1	30–37
May/Jun 2010	236–322	−92 to −41	−10.1 to −8.4	23–38
Sep 2010	38–43	−54 to −50	+6.3 to +6.9	29–32
May/Jun 2011	267–302	−61 to −40	−10.1 to −8.6	34–38
Jul 2011	144–150	85–88	+5.2 to +5.8	10–14
Jun 2012	40–108	33–76	+6.6 to +10.1	29–38
Sep 2012	118–131	17–23	+7.1 to +8.4	20–26
May 2013	282–52	−32 to 51	−9.8 to +7.7	9–38
Jun 2013	147–157	115–122	+4.3 to +5.3	6–11

the Sun, R, and on the Doppler shift (Smyth, 1986). We adopt the g factor computed in Killen et al. (2009). We assume, as in Cassidy et al. (2015), that the sodium atoms are nearly at rest with respect to Mercury. This assumption fails where the Na atoms have a not negligible relative velocity with respect to Mercury, for example in the tail. Since we are analyzing only disk images, the assumption is almost valid. The g-factor can be written as

$$g = F_s(\lambda + d\lambda)\cdot\sigma(\lambda)\cdot\lambda\cdot\frac{Vr}{c} \tag{1}$$

where $F_s(\lambda)$ is the solar differential flux function at the wavelength λ, V_r is Mercury's radial velocity with respect to the Sun, and c is the speed of light, and $\sigma = 0.6\ 10^{-11}$ cm^2 is the cross section for auto-absorption at high temperatures.

Note that the dependence of g factor from the true anomaly angle of Mercury is implied in two ways: F_s is proportional to the inverse of the square of the distance from the Sun, but it is also shifted by $d\lambda$, which in turn depends on the radial velocity V_r which again depends on the solar zenith angle and has maxima (in absolute value) for true anomaly of ~60° and ~ 300°.

Both Vr and g factor are over plotted to the observed Na D2 emissions in Fig. 2 and the computed ranges for each period are listed in Table 1.

The conversion between observed radiance, I, and column density, N, along the line of sight, in the case of optically thin column density, is given by the formula:

$$N = \frac{I}{g}10^6 \tag{2}$$

The factor 10^6 takes into account the fact that radiance is in rayleigh (10^{10} photons m^{-2} s^{-1}) and column density is in cm^{-2}.

In the case of optically thick line, we consider that the observed column density is obtained by the emission generated by the real column density absorbed along the line of sight.

$$N = \int_0^{N_c} exp(-n\sigma)dn = \frac{I}{\sigma}\left(1 - exp\left(-N_c\sigma\right)\right) \tag{3}$$

The corrected column density, N_c, is

$$N_c = \frac{-ln(1 - N\sigma)}{\sigma} \tag{4}$$

This correction neglects multiple scattering that would produce a higher emission (so a lower correction with respect the optically thin case), that should be considered when N approaches $1/\sigma = 1.6\ 10^{11}$ cm^{-2}. This maximum-allowed value is close to the values obtained in the equatorial region approaching the aphelion.

The correction due to photon multiple scattering has been estimated in the appendix of Cassidy et al. (2015). According to their estimation, the real column density is

$$N_r = \frac{N}{\left(F - \frac{1-F}{4}\right)} \tag{5}$$

where F is the fraction of photons not scattered inside the column:

$$F = \left(1 - e^{-N\sigma}\right)/N\sigma \tag{6}$$

In this case, for $N = 1/\sigma$, $N_r = 1/\sigma$ (1–5/4e)

We note that, even if the column densities for higher values are reconstructed with some more indetermination, and that we are neglecting the positive feedback in g-value on the outbound leg and the negative feedback on the inbound leg as described in Potter et al. (2007), the main results of the present study are not affected by them.

Finally, the computed column density refers to the line of sight of the observation. This is a limitation in the following analysis since for a correct comparison a zenith column density should be considered. This correction can be done only when the disk pixels are considered and by knowing the scale height of the exosphere. The scale height, ranging between 80 and 100 km in the subsolar point (Cassidy et al., 2015), is influenced by the surface release processes, by radiation pressure, by thermal accommodation and other processes like photoionization, so it depends by planetographic positions and by TAA. For this reason, we consider the line-of-sight column densities with the caveat that they have probably a positive bias for the pixels at the limb.

3.2. Latitudinal distributions

We divided the images into three regions: equatorial region $-0.3\ R_d < r < +0.3\ R_d$, northern region $r > 0.3Rd$ and southern region $r < 0.3\ R_d$, where R_d is the observed planetary disk radius. In Fig. 1 some examples of observations are shown with the visualization of the above defined regions.

For each region, we computed the average emission per pixel (Ep) by considering only pixels inside the circle of 1.3 R_d with an intensity above a threshold defined as half of the average of the whole image. Since in a few cases we see spiky pixels, probably related to non- optimal removal of the cosmic rays detection, we cleaned the images removing pixels with intensity above average + 3 std. of the adjacent pixels.

The result of this first analysis is shown in Fig. 2 where average Na emission is plotted vs TAA. As already showed in previous studies (Leblanc and Johnson, 2010) the global emission follows roughly the g factor trend (magenta line in Fig. 2) along the Mercury's orbit. Unfortunately, the low g factor in the perihelion and aphelion sector produce a lack of coverage in TAA of the observations. We can notice that the emission is highly variable also at fixed TAAs. The plot seems to highlight that the northern emission is generally higher from the perihelion toward TAA = 135°, while the southern emission seems higher in the TAA range 225°-315°. The emission in the equatorial region is higher while approaching the aphelion.

The resulting column densities divided by North, Equator and South regions compared to average column density in the full disk (black circles) are shown in Fig. 3. These plots show that there is a general increase in Na exosphere soon after the perihelion, picking at about TAA 30°, and even more approaching the aphelion, this is true for all the three latitudinal regions but especially for the equatorial one (central panel). This result, first noted by Potter et al. (2007) is in good agreement with the MESSENGER result reported by Cassidy et al. (2015), where the aphelion maximum is explained as related to the position along the Mercury orbit where the loss rate of the Na exosphere is the lowest, since at these TAAs also the radiation acceleration and photoionization rate assume the lowest values. At perihelion the secondary maximum was explained by considering a minimum radiation

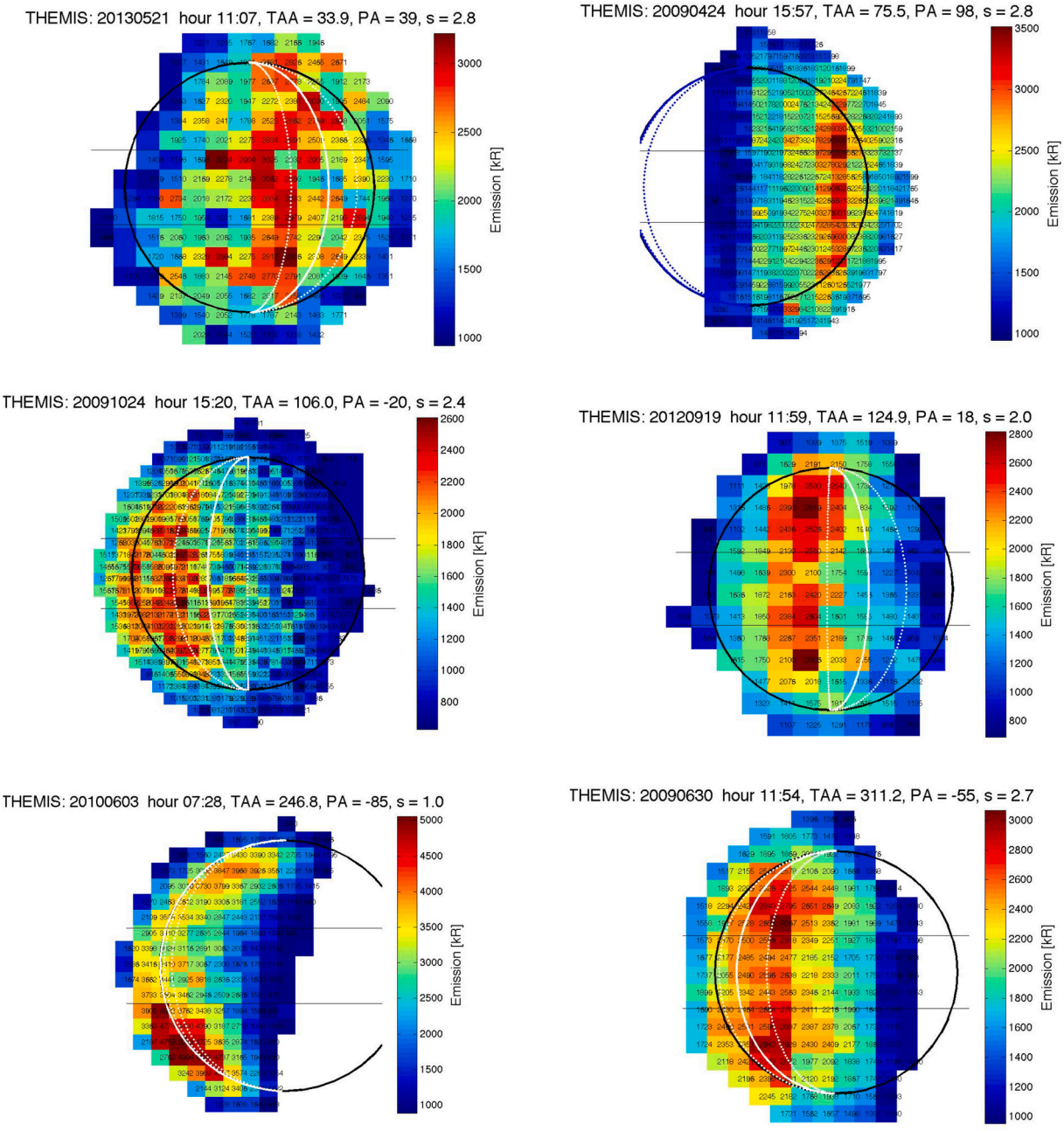

Fig. 1. Examples of analyzed THEMIS images. The solid black circle is the planet disk. The light black horizontal lines delimit the latitudinal regions. The white solid curve shows the subsolar longitude, while the dotted white lines show the + and −20° longitudes from the subsolar one. The blue dotted lines in the second image show the + and −20° longitude from the anti-subsolar longitude (blue solid curve), since in this case the subsolar point is not visible from the Earth. (For interpretation of the references to colour in this figure legend, the reader is referred to the web version of this article.)

acceleration, but highest photoionization rate. We notice that the secondary pick, being not exactly at the perihelion, but at TAA 30°, could be also related to the comet Encke/2P stream crossing (Killen and Hahn, 2015), so it could be the signature of the predominant surface release due to micrometeoroid impact vaporization in this period of the year.

In addition, in Fig. 3 the latitudinal column density variability with respect to the disk average is clearly visible. The Northern densities are above the average one between TAA 0° and 120°. The equatorial densities are generally higher or similar to the disk average, but strongly higher at 120° < TAA < 180°. Finally, the southern regions densities are higher than the average disk values in the second half of the year.

According to Orsini et al. (2018), we know that two CMEs passed at Mercury on 20th September 2012 and they seemed to produce a change in the exosphere configuration, showing a more spread Na distribution picking at the equatorial latitudes. In Fig. 3, we highlight this event, which in principle could have a behavior out of the "nominal" exosphere, by plotting the observations of this day (at TAA = 128°) with stars. We can say that the general trend due to the position of Mercury along the orbit is predominant with respect to the effect possibly induced by space weather.

A direct comparison between the northern and southern column densities is shown in Fig. 4, where the two distinctive regimes during the two halves of the Mercury year are clearly evident.

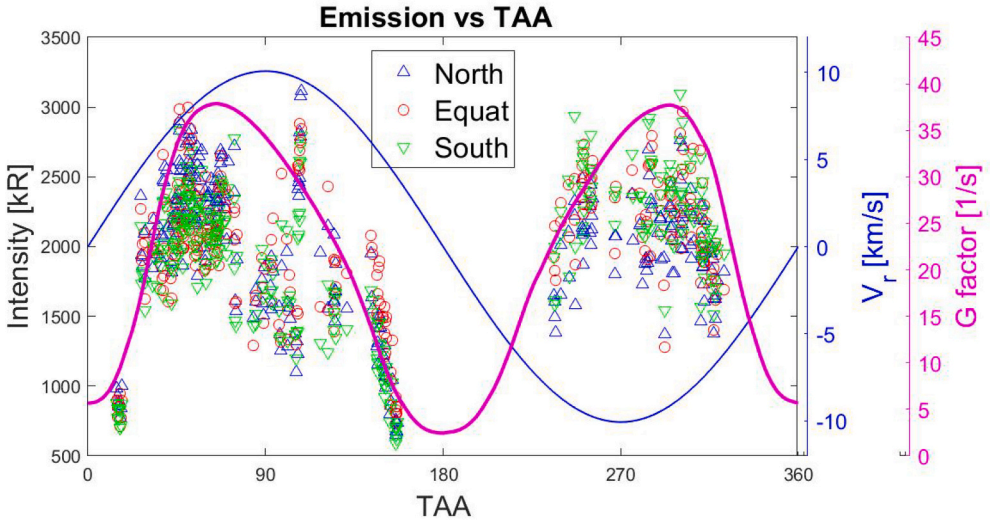

Fig. 2. Average Na emission/pixel in the whole disk, in the North, Equator and South regions along the Mercury's year. The blue curve (see right axis) shows the radial velocity and the magenta curve shows the trend of g-factor along the Mercury's orbit. (For interpretation of the references to colour in this figure legend, the reader is referred to the web version of this article.)

3.3. Local time distributions

In order to investigate dawn and dusk asymmetries, the equatorial emission has been further analyzed.

In this analysis, only the equatorial region inside the disk ($< 1\ R_d$) has been considered to limit the analysis to the line-of-sights crossing the Na exosphere just above the surface, so avoiding mixing too different integration paths; in fact, the line-of-sights lying outside the planetary disk are about twice. The equatorial band has been divided into 3 longitudinal ranges: longitudes $>20°$ from subsolar longitude (postnoon, i.e. duskward), longitudes $<20°$ from subsolar longitude (prenoon, i.e. dawnward) and subsolar region between $\pm 20°$ (see Fig. 1, white curves).

Not all THEMIS images simultaneously show the dawnward and the duskward hemispheres, and often one of the two is covered by only few pixels, because of the high phase angle. Hence, we decided to consider a statistical limit for this analysis, that is, we accepted the average value of one region only if at least 8 pixels are visible inside the planetary disk.

Even if only few images allow the simultaneous dawn-dusk comparison, we can compare the dawn and dusk emission with the sub-solar (SS) region, and obtain a statistical result. In Fig. 5 upper panel, the column densities obtained for the three longitudinal equatorial regions are shown vs TAA. We can see that along the whole perihelion half year (between $\pm 90°$ TAA) the column density of the SS region is generally higher than the other two. On the other hand, it is clear that at TAA about 90° the duskward emission is lower than the dawnward one and approaching the aphelion the dawn emission is also higher than the SS one. Unfortunately, regarding the observations at TAA between 225°–260° only observations with the visible duskward hemisphere are available in our data set.

To better focus on the asymmetries, we compute, where possible, the difference between the dawn or dusk emission and the SS emission. Note that we decided to analyze the differences and not the ratios because we consider the interpretation of the positive and negative differences easier. The result is shown in Fig. 5 bottom panel. We can see that the differences for dawnward and duskward regions are almost always negative along the year, confirming that the SS densities are higher. This is what we can expect by considering higher photon flux and a column density dependent mainly by the solar illumination with a minor role of the surface composition. Here we should note that the line-of-sight column densities have a geometrical bias that increases the values for the pixels at limb, and the SS regions are generally at the limb. In Fig. 5 bottom panel, there is a clear bifurcation of duskward decrease and dawnward increase above 0 at TAA approximately between 90 and 150°. This is the period of the Mercury year when the cold pole, described by Cassidy et al. (2016), "sees" the sunrise.

We investigate whether the result obtained with the dawnward emission much higher than the SS one is due to a single specific run of observations. There are three observation campaigns covering the TAA between 90° and 150°: October 2009 (TAA between 70° and 110°), June 2012 (TAA about 110°) and September 2012 (TAA 110°–140°). In Fig. 1, two typical images of the periods are shown. The latter is the period analyzed also in Orsini et al. (2018) where the CME was approaching. Hence, we can conclude that this is a recurrent behavior, to be observed every year.

Indeed, also the analysis of the ground-based observations data set of Potter et al. (2006) obtained between 1997 and 2003, showed a higher terminator to limb ratio when the dawn hemisphere was in view for TAA between about 20° and 120°. This is in agreement with our analysis, nevertheless the ratio was almost always greater than 1 for dawn hemisphere in view, thus showing that usually the dawn terminator density was higher than the one at the limb. Even if it is not an exact comparison between subsolar density and dawnward density, their analysis depicts an equatorial seasonal variability driven by a release in the surface as soon as it is illuminated by the Sun and a relatively fast depletion.

4. Discussion

Figs. 3, 4 and 5 show a clear seasonal modulation of the global Na exosphere visible at all the considered regions at different latitudes and local times, ranging between 0.5 and 2.5×10^{11} atoms/cm^2. There is a general spread of the data of about 25% of the total variability along the year. This means that while the seasonal variability is dominant, there is also a variability not associated to the orbital position. Therefore, we can assert that this study does not exclude that there is also a short time-scale variability due to plasma precipitation modulated by solar wind, IMF conditions and solar events, like CMEs (e.g: Mangano et al., 2013; Orsini et al., 2018).

The global Na content in the exosphere is maximum when approaching the aphelion where both the radiation pressure and solar photon flux are minimum, and therefore, also the loss rate is minimum. But given the minimum value of the g-factor at aphelion, performing observations is much more difficult, and consequently there are no data. At perihelion a secondary maximum is observed (Fig. 3) that can be

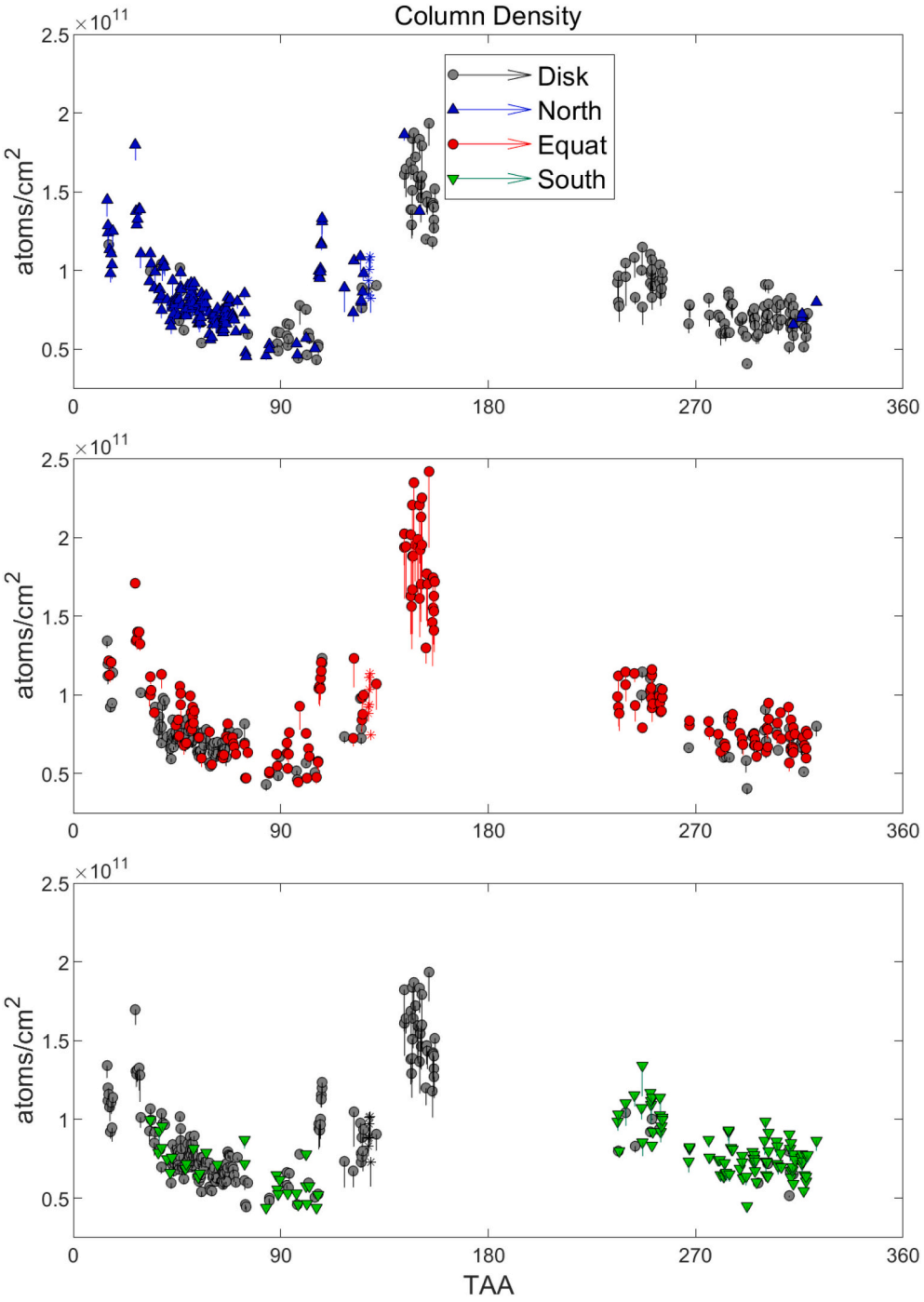

Fig. 3. Average Na column density obtained from the THEMIS images along the Mercury's year, divided by latitudinal regions: North (above), Equator (middle) and South (below). The arrows range from the considered region to the average disk column density if the region is higher than the disk average, while the arrows range from the disk average (grey dots) to the region average if the region is lower than the disk. At about TAA 128, the 20th September 2012 data, taken during CME passages at Mercury, are marked as stars.

explained as a consequence of the combination of decrease of the radiation pressure, together with the maximum of photon flux at such minimum solar distances, producing a maximum Na atoms photoionization rate. This result is in good agreement with the analysis of the MESSENGER observations of the subsolar density obtained between 2011 and 2013 (Cassidy et al., 2015) and with the analysis of normalized (at a specific TAA) average Na D2 emission obtained from McMath-Pierce observations between 1997 and 2003 by Potter et al. (2007).

The global increase of the column density when approaching the aphelion is maximum in the equatorial region (Fig. 2 middle panel). This effect could be put in relation with the high values we observed in the dawn sector (Fig. 5 upper panel), even if we actually don't have dusk data after TAA about 110°. If this is true, it can be explained with an extra contribution coming from a new source at the surface, i.e. the free Na accumulated in the cold pole while it was in the night side (Cassidy et al., 2016).

Our data set includes mostly eastern elongation (when the Sun is seen on the right side of Mercury and the dawnward hemisphere is in view) in the first half of the year and almost only western elongation (duskward hemisphere in view) in the second half of the year. Unfortunately, the few data between TAA 150° and 250° are not sufficient to investigate any possible dusk column density prevalence with respect to dawn one, as expected according to the Cassidy et al. (2016) analysis of MESSENGER data, but not confirmed by the analysis of the Potter et al. (2006) ground-based data set.

In Fig. 6 upper panel, a summary sketch is drawn for the equatorial

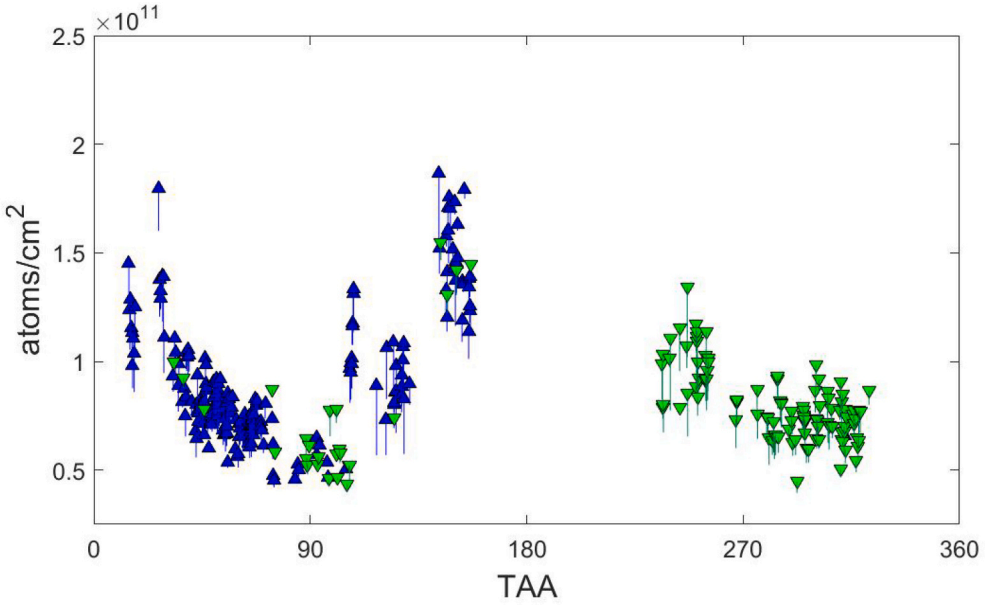

Fig. 4. Average Na column density along the Mercury's orbit. The green arrows range from South (green triangles) to North column densities, while the blue arrows range from North (blue triangles) to South column densities. (For interpretation of the references to colour in this figure legend, the reader is referred to the web version of this article.)

column density local time asymmetries obtained from our analysis as in and Fig. 5 upper panel. Our analysis shows that the subsolar column density is higher than the equatorial emission at dawn or at dusk in the perihelion half year ($-90° < TAA < +90°$), but we cannot exclude that this is partially due to the fact that in this analysis the line-of-sight column densities are considered instead of the zenith column densities. At TAA between 90° and 150° the dawn column density is prevalent. This seems a different local time relative behavior with respect to the results obtained by other data sets. Potter et al. (2006) data subset of dawn view images showed a terminator/limb ratio (thus dawnward/midday ratio) greater than one along almost the whole year and equal to about one between TAA 140° and 250° and close to perihelion (see Fig. 4 in Cassidy et al., 2016). Their analysis showed that for data subset of dusk view images the terminator/limb (thus duskward/midday) ratio is always about unity with a decrease to 0.5 at about TAA = 100°. However, it must be noted that while our comparison considers the equatorial SS region, their limb values could be related to local times dependent on the phase angle of the observation.

The ratio of the MESSENGER/MASCS derived surface densities at 8 LT and 16 LT out of 12 LT, resulted greater than 1 during almost the whole year, and below 1 close to the aphelion period between 160°–250° for 8/12 and 100°–210° for 16/12, respectively (see Fig. 4 of Cassidy et al., 2016). According to their analysis, the reservoir of condensed Na onto the surface seems to play a major role with respect to the trend of photon flux intensity along the main part of the Mercury's year, in fact the subsolar density is the highest only when the cold pole is close to noon.

The comparison of our results, Fig. 5 bottom panel, with the MESSENGER/ MASCS ones **(Cassidy et al., 2016)** shows a general agreement of the 8/12 and 16/12 LT density ratio up to TAA 110°, that is, the Na content at dawn increases monotonically with respect to the subsolar one, while the dusk content follow the dawn trend up to TAA 70° and then decreases abruptly. According to MASCS and McMath-Pierce analysis also the Na dawn/noon content should decrease approaching the aphelion. A steep decrease of the dawn column density can be seen also in our data (Fig. 5 upper panel) at $145° < TAA < 160°$, but these observations were performed during a large phase angle geometry, not allowing for a comparison with the subsolar region. Anyway, the decrease of the 8/12 LT ratio for MASCS data starts earlier at about TAA = 100° (**Cassidy et al., 2016**).

In the second half of the year our data analysis does not show any clear trend, the dawn – SS data are too few and the dusk - SS data at $260° < TAA < 320°$ do not show any trend as the Potter et al. (2006) data, but we can note that the dusk densities are lower than the SS ones. In the same orbit phase the MASC 16/12 density ratios show a maximum at about 270° and a decrease toward the perihelion. Furthermore, **Cassidy et al. (2016)** showed that also the 8/12 density ratios has a secondary maximum at about TAA = 300°, thus the SS density is lower than the other LTs also in the perihelion phase.

In general, we can conclude that, at about $90° < TAA < 150°$, when a cold surface region is brought to solar illumination at dawn and the antipodal region (already depleted from volatiles) sees the sunset, the Na equatorial distribution shows clear dawn prevalence exceeding the subsolar exosphere and a dusk decrease. This asymmetry is confirmed by the three different data sets.

When the so-called cold pole is toward dusk the present available ground-based data set cannot confirm that the Na release is still higher at the same region. In contrast, according to our results, along the perihelion half year the subsolar exosphere is the highest (Fig. 6 upper panel).

In the statistical analysis of Mangano et al. (2015), the northern emission was found to be predominant when dawnward hemisphere was in view (eastern-elongation), while the southern peak emission dominated when duskward hemisphere was in view (western elongation). It must be stressed that the THEMIS data contains mostly eastern-elongated (dawn hemisphere) observations during the first half of Mercury's orbit (that is, from perihelion to aphelion), and western-elongated (dusk hemisphere) observations on its second half (aphelion to perihelion).

Hence, in the present study, we find also a seasonal dependence, showing a northern peak prevalence in the outbound part of the orbit and a southern peak prevalence in the in bound part (mainly dusk-view observations), but - given the available data set - we cannot claim whether the northern/southern dominant emission is related to the pre−/post-aphelion phase or to the dawn/dusk hemisphere view. In Fig. 6 bottom panel, a qualitative summary is drawn for a better visualization of the column density latitudinal prevalence compared to the disk average along the orbit. Under the reasonable assumption that the

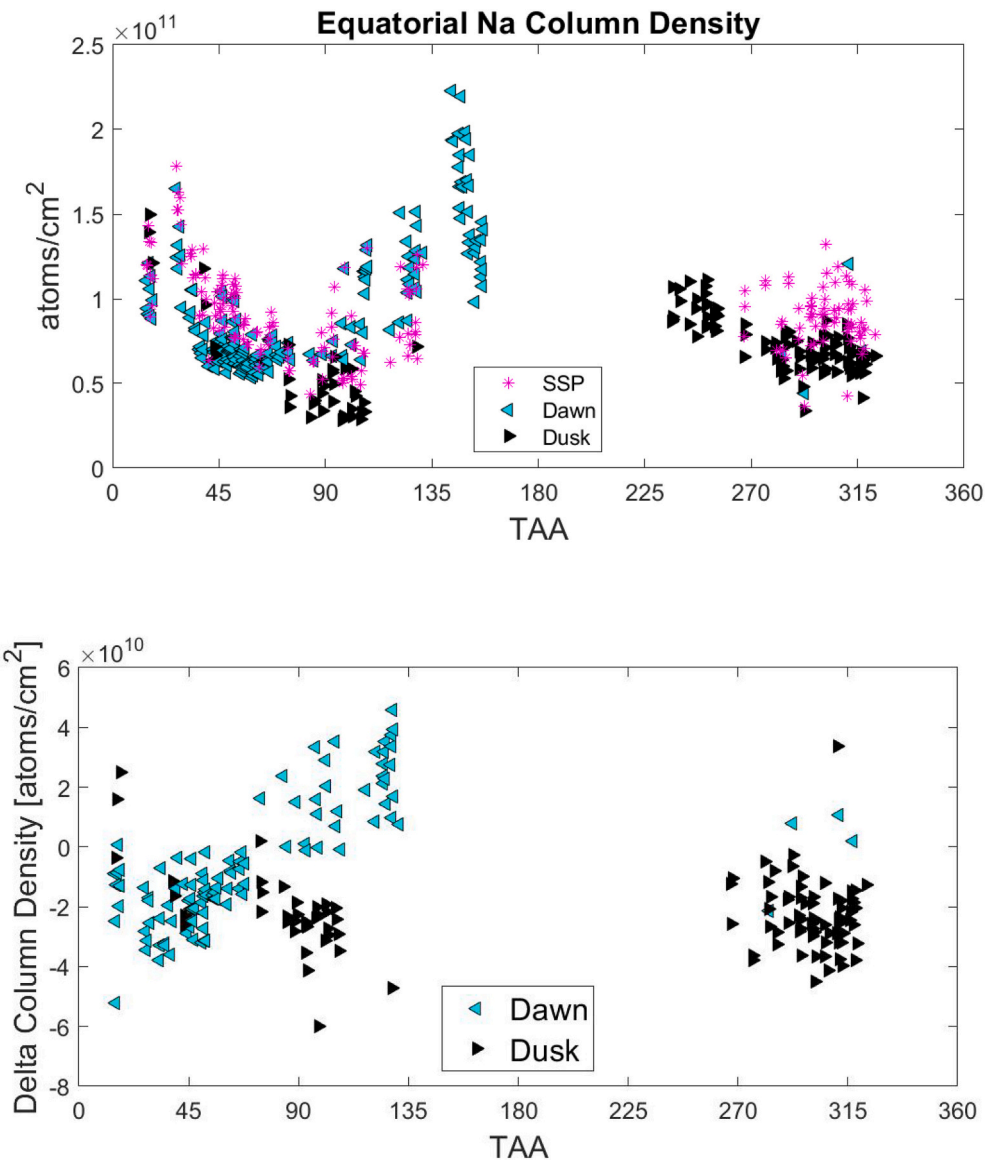

Fig. 5. Upper panel. Equatorial disk (<0.3 Rd from the equator and inside the circle 1Rd) THEMIS Na column density along the Mercury's year, divided by longitudinal regions: dawn (<−20° from SS longitude) (cyan triangles), SS (between −20° and + 20°) (magenta stars) and dusk (>20° from SS longitude) (black triangles). Bottom panel. Difference between equatorial disk Na column densities of dawnward regions and of SS (cyan square) and between Na column densities of duskward and SS (black square) obtained from the THEMIS data set. (For interpretation of the references to colour in this figure legend, the reader is referred to the web version of this article.)

mid-high latitudes emission is caused by the solar wind precipitation through the cusps, this local time vs latitude relation could be tentatively explained with a significant dawnward/duskward dislocation of the northern/southern cusp induced by a quasi-steady IMF By > > 0 (Massetti et al., 2003). Nevertheless, this effect seems to be excluded by the analysis of the quasi-full disk images (THEMIS dataset), where both hemispheres are in view, which show a substantial meridional alignment of the northern and southern peaks (Mangano et al., 2015); moreover, this systematic tilt has not been reported by MESSENGER.

We also checked a possible relation of the Na column density with the distance from the ecliptic plane, where the dust distribution is higher (Mann et al., 2004). In fact, the Mercury's orbit has an inclination angle of 7° with respect to the ecliptic, and it is above the interplanetary disk between TAA −45° and 135° and it is below between TAA 135° and 325° (Fig. 6 bottom panel). This means that when Mercury is above the dust disk the northern peak is the predominant one, while the southern peak is higher when Mercury is below. Hence, this analysis seems to indicate that, if there is a relation between the Na exosphere and the dust, it is an anticorrelation, thus the micrometeoroid impact vaporization should not be the major contribution for the Na exosphere generation at high latitudes. This goes against the results found by Kameda et al. (2009) that concluded that the disk global Na column density is higher when Mercury cross the dust disk. Nevertheless, we must note that Mercury's orbit ranges within few degrees of ecliptic latitudes, while the dust disk extends to higher latitudes. A thorough analysis needs to be done considering intensity, direction and speed of the dust flux to the surface.

Potter et al. (2006) analyzed the occurrence of southern or northern peak along the Mercury's orbit and concluded that there is not any obvious relation with TAA. They found that for the dawn observations there is a prevalence of southern peak, while the peaks are uniformly distributed between north and south in the case of dusk observations. By looking deeply their Fig. 14, we see that in the first half year the north/south ratios assume higher values for dawn observations, except for TAA = 0°–40° where dusk values are almost above one and dawn are below 1. In the second half of the year (180° < TAA < 300°) their data set lacks dusk observations, so the Southern pick prevalence could be related to most of observation at dawn in the inbound part of the orbit.

Finally, we can conclude that their data set slightly agree with our analysis showing a northern peak at higher values for the dawn observations during the first half of the orbit. The dusk North/South ratio shows northern prevalence only at TAA < 40, on the contrary it seems that this ratio is prevalently < 1 for 60° < TAA < 150°. It is more difficult to recognize similar southern peak prevalence in the second half of the year. The opposite with-respect-to-ours relation between the dawn view

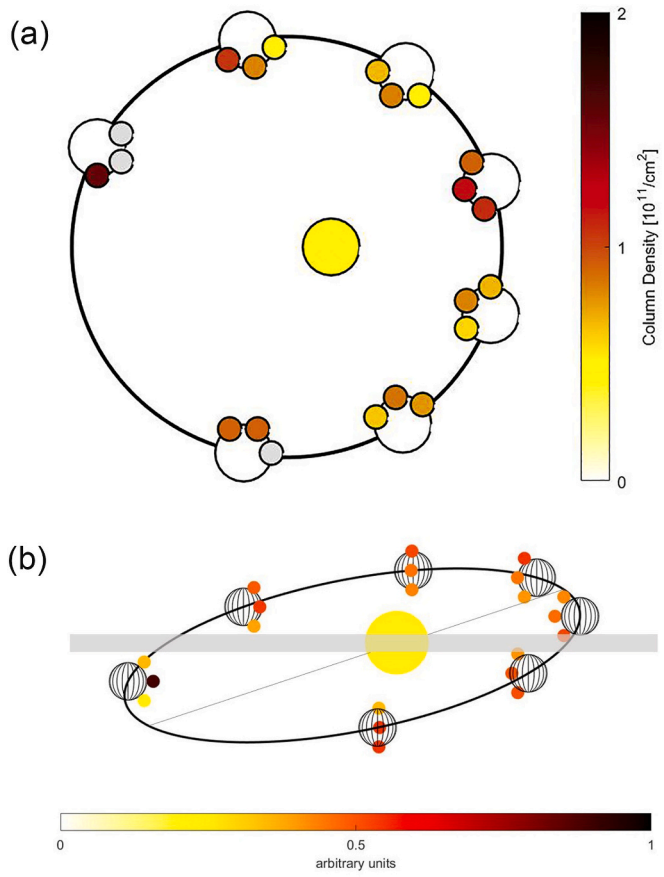

Fig. 6. Upper panel: schematic view of the equatorial LT asymmetries of the Na column density along the Mercury's orbit obtained from the THEMIS data set. Grey bullets represents no data available. Bottom panel: qualitative representation of the latitudinal column density with respect to the disk average obtained by the THEMIS data set. The shadowed area represents the dust disk in the ecliptic plane. The thin line shows the apses line. The Mercury's orbital inclination is amplified to highlight the regions above and below the ecliptic plane.

and the southern peak obtained from their data set could suggest the presence of some kind of bias in one or both the datasets, possibly linked to the uneven coverage of the whole orbit.

We speculated also on a possible relation with other external environment conditions, for example, checking the possibility that the displacement of the planet along different solar latitudes (above and below the ecliptic) could produce a different ion precipitation pattern due to different interplanetary conditions, as solar polarity. In fact, while the interplanetary magnetic filed varies at timescales less than minutes, having the sign of the IMF Bz_{MSO} component on average 0 nT, the IMF Bx_{MSO} component follows the heliospheric current sheet wrapping which has a variability at longer timescales and sign averages following the solar cycle. This could induce some statistical effect. We notice that the MESSENGER/MAG data analyzed in Mangano et al. (2015) showed a prevalence in IMF $Bx_{MSO} > 0$ nT component, better related to double peak North profiles, but that analysis was done for only 3 years, i. e. 2011–2013, when MAG data were available. The Potter et al. (2006) data set was collected between 1997 and 2003, that is, during the previous solar cycle 23, when the IMF polarity was opposite. So, if there is any relation with the IMF polarity, it should be reversed for the two data sets for positions above or below the ecliptic plane. Finally, we cannot find any clear indication in this direction, and the IMF orientation is highly varying along the solar cycle, being well organized in two hemispheres only during the solar minimum.

Considering that the different configurations seems also related to the inbound and outbound legs of the orbit, we can notice that in these two orbital legs the Mercury's radial velocity has a quite different effect on the radiation acceleration, as noted by Potter et al. (2007). The radiation acceleration sums to the radial velocity (positive feedback) in the outbound leg, conversely, during the inbound leg Mercury's radial velocity is subtracted to the radiation acceleration (negative feedback). In other words, at same values of the radiation acceleration the exospheric particles are pushed anti-sunward also depending on the TAA. In principle, this should not produce a latitudinal effect; nevertheless, detailed modeling of the exosphere dynamics could help in this investigation.

5. Conclusions

The analysis of THEMIS observations versus the TAA presented in this study confirms some previously obtained results from space and ground based observations, but it also shows some differences and unexplained features.

The seasonal modulation of the Na column density (0.5–2.5 10^{11} atoms/cm^2) shows a general spread of the data accounting for a short time-scale variability probably due to plasma precipitation modulated by IMF configuration and solar events (e.g.: Mangano et al., 2013; Orsini et al., 2018).

The global Na content in the exosphere is maximum approaching the aphelion with a secondary maximum at perihelion, as already noticed by previous work. This can be explained by the global Na loss rate variation along the Mercury's orbit. Our analysis supports the idea that an equatorial region, the so-called "cold pole", produces a noticeable increase of the Na release when it starts to be illuminated by the rising Sun, at $70^\circ < TAA < 150^\circ$, as suggested by Cassidy et al. (2016). Such an increase is recognizable in less extent in our dataset at all the latitudinal regions.

The THEMIS data set analyzed in the present paper, as the one of Potter et al. (2006), cannot confirm the outcome of Cassidy et al. (2016) that the cold pole maintains the higher Na release rate when it is in the afternoon sector (after crossing the sub-solar region, that is, after aphelion).

This study shows that the sub-solar exosphere is generally higher with respect to other local times, with the exception of the period when the cold region is at dawn. The supported scenario, then, is that there is a migration of Na toward the night side with a preferential condensation on the coldest surface, but the Na reservoir is depleted and the condensed atoms are redistributed when the surface is back in the sunlight.

The analysis of the northern and southern peaks along the year in relation to the local time showed an unexpected behavior that is not easy to explain and that do not fully agree with the analysis obtained with the McMath Pierce data set (Potter et al., 2006). In fact, the present study shows a clear northern peak prevalence in the orbit outbound leg (from perihelion to aphelion), and a southern major peak in the inbound leg (from aphelion to perihelion). These results seem to be not supported by previous analyses by Potter et al. (2006), even if this could be related to a different coverage of the data along the orbit.

The analysis of the dusk observations shows a southern peak prevalence. The apparent relation between the northern peak and the dawnward hemisphere images could be just due to the absence of dawn observations in the second half of the year. In fact, this relation is not confirmed, on the contrary, it is the opposite in the Potter et al. (2006) data set.

The explanation of this seasonal peak variation is not straightforward. It seems not due to the impact of the dust, and neither to solar polarity. Anyway, possible implications in Na exosphere induced by the variation of the solar radiance or IMF polarity due to solar cycle phases or differences among different solar cycles (e.g.: Hathaway, 2015) needs further analysis. Also a possible link to the different effects of the radiation acceleration along Mercury's orbit needs further investigation

with detailed models of exosphere dynamics.

When comparing the three available data sets from THEMIS, from McMath Pierce Earth based solar telescopes, and from MESSENGER/MASC spectrometer, we should take into account that we consider the line of sight column densities, the Potter et al. (2006) data set consider the ratio of the emissions, while the MASCS data (Cassidy et al., 2015, 2016) considers the exosphere density at the surface. This could produce some differences in the conclusions since the exospheric scale height is dependent on the active surface release process, radiation pressure, thermal accommodation and sticking, and other processes in the exosphere itself. Lower scale heights (less energetic surface release processes) result in higher densities at the surface. Nevertheless, since the two quantities are proportional, as a first analysis we think that the comparison is surely valuable.

The present study showed that further observations from ground and from space are both necessary to solve the presented open issues of Na exosphere asymmetries. In the next years, ground based observations of the Na exosphere at different elongations and TAAs, filling the gap in TAA coverage are recommended. In addition, the next outcomes from the BepiColombo mission, launched in 2018, (Benkhoff et al., 2020) are truly desired, since it will observe the Na exosphere emission with a dedicated imager (MSASI on board of the Mio spacecraft), and at the same time the local exosphere density with the mass spectrometer SERENA-STROFIO (on board the MPO spacecraft). The possibility to have simultaneous measurements of dust distribution, of precipitating ions and magnetic field configuration, coupled with surface compositional maps, will provide information on possible drivers of the Na release and, hopefully, solve the open issues of exospheric generation and dynamics (Milillo et al., 2020). Moreover, the existence of simultaneous multi-instrument and multi-point measurements during BepiColombo will show the role of transient solar events in the Na release in Mercury's exosphere. Eventually, investigating the planetary space weather in Mercury's environment (see, for instance, discussion in Plainaki et al., 2016) will help to disentangle the effect of different drivers in the exosphere distribution and possibly to better interpret seasonal and short-term variabilities in the Na exosphere.

Declaration of Competing Interest

None.

Acknowledgments

This work was supported by the ASI-INAF agreement no. 2018-8-HH.O "Partecipazione scientifica alla missione BEPICOLOMBO SERENA Fase El". Ground-based observation campaign of Mercury's Na exosphere from THEMIS was started and organized by F. Leblanc; the INAF participation is led by V. Mangano. Data are available online at "http://themis.iaps.inaf.it". Authors thank the THEMIS staff in Tenerife (Canary Islands, Spain) for their fruitful help during the observation campaigns. For THEMIS data in 2013, this research received financial support from the European Union's Horizon 2020 research and innovation program under grant agreement N. 824135 (SOLARNET). The authors thank the referees for helping to improve this article.

References

Benkhoff, et al., 2020. BepiColombo Special Issue SSR. submitted.
Cassidy, T.A., Merkel, A.W., Burger, M.H., Sarantos, M., Killen, R.M., McClintock, W.E., Vervack, R.J., 2015. Mercury's seasonal sodium exosphere: MESSENGER orbital observations. Icarus 248, 547–559. https://doi.org/10.1016/j.icarus.2014.10.037.
Cassidy, T.A., McClintock, W.E., Killen, R.M., Sarantos, M., Merkel, A.W., Vervack, R.J., Burger, M.H., 2016. A cold-pole enhancement in Mercury's sodium exosphere. Geoph. Res. Lett. 44 https://doi.org/10.1002/2016GL071071.
Hathaway, D.H., 2015. The solar cycle. Living Rev. Sol. Phys. 12, 4. https://doi.org/10.1007/lrsp-2015-4.
Kameda, S., Yoshikawa, I., Kagitani, M., Okano, S., 2009. Interplanetary dust distribution and temporal variability of Mercury's atmospheric Na. Geophys. Res. Lett. 36, L15201 https://doi.org/10.1029/2009GL039036.
Killen, R.M., Hahn, J.M., 2015. Impact vaporization as a possible source of Mercury's calcium exosphere. Icarus 250, 230–237.
Killen, R.M., Ip, W.H., 1999. The surface-bounded atmospheres of Mercury and the Moon. Rev. Geophys. 37, 361–406.
Killen, R.M., Potter, A.E., Reiff, P., Sarantos, M., Jackson, B.V., Hick, P., Giles, B., 2001. Evidence for space weather at Mercury. J. Geophys. Res. 106, 20509–20525.
Killen, R.M., Shemansky, D., Mouawad, N., 2009. Expected emission from Mercury's exospheric species, and their ultraviolet–visible signatures. Ap. J. Suppl. Ser. 181, 351–359.
Leblanc, F., Johnson, R.E., 2003. Mercury's sodium exosphere. Icarus 164, 261–281. https://doi.org/10.1016/S0019-1035(03)00147-7.
Leblanc, F., Johnson, R.E., 2010. Mercury exosphere. I. Global circulation model of its sodium Component. Icarus 209, 280–300.
Leblanc, F., et al., 2008. High latitude peaks in Mercury's sodium exosphere: spectral signature using THEMIS solar telescope. Geophys. Res. Lett. 35, 18. https://doi.org/10.1029/2008GL035322.
Leblanc, F., et al., 2009. Short-term variations of Mercury's Na exosphere observed with very high spectral resolution. Geophys. Res. Lett. 36, 7. https://doi.org/10.1029/2009GL038089.
Leblanc, F., Chaufray, Y.-Y., Doressoundiram, A., Berthelier, J.-J., 2013. Mercury exosphere. III: Energetic characterization of its sodium component. Icarus 223 (2), 963–974.
López-Ariste, A., Rayrole, J., Semel, M., 2000. First results from THEMIS spectropolarimetric mode. A&AS 142, 137–148. https://doi.org/10.1051/aas:2000144.
Mangano, V., Massetti, S., Milillo, A., Mura, A., Orsini, S., Leblanc, F., 2013. Dynamical evolution of sodium anisotropies in the exosphere of Mercury. Planet. Space Sci. 82–83, 1–10.
Mangano, V., Massetti, S., Milillo, A., Plainaki, C., Orsini, S., Leblanc, F., 2015. THEMIS Na exosphere observations of Mercury and their correlation with in-situ magnetic field measurements by MESSENGER (Special Issue). Planet. Space Sci. 115, 102–109. https://doi.org/10.1016/j.pss.2015.04.001.
Mann, I., et al., 2004. Dust near the Sun. Space Sci. Rev. 110, 269–305. https://doi.org/10.1023/B:SPAC.0000023440.82735.ba.
Massetti, S., Orsini, S., Milillo, A., Mura, A., De Angelis, E., Lammer, H., Wurz, P., 2003. Mapping of the cusp plasma precipitation on the surface of Mercury. Icarus 166 (2), 229–237. https://doi.org/10.1016/j.icarus.2003.08.005.
Massetti, S., Mangano, V., Milillo, A., Mura, A., Orsini, S., Plainaki, C., 2017. Short-term observations of double peaked Na emission from Mercury's exosphere. Geoph. Res. Lett. 44 (7), 2970–2977. https://doi.org/10.1002/2017GL073090.
McClintock, W.E., Lankton, M.R., 2007. The Mercury atmospheric and surface composition spectrometer for the MESSENGER Mission. Space Sci. Rev. 131, 481–521. https://doi.org/10.1007/s11214-007-9264-5.
Mein, P., Rayrole, J., 1985. Themis Solar Telescope, Vistas in Astronomy, vol. 28. Elsevier, Amsterdam, p. 567. https://doi.org/10.1016/0083-6656(85)90077-7.
Milillo, A., Fujimoto, M., Kallio, E., Kameda, S., Leblanc, F., Narita, Y., Cremonese, G., Laakso, H., Laurenza, M., Massetti, S., McKenna-Lawlor, S., Mura, A., Nakamura, R., Omura, Y., Rothery, D.A., Seki, K., Storini, M., Wurz, P., Baumjohann, W., Bunce, E. J., Kasaba, Y., Helbert, J., Sprague, A., Hermean Environment WG, 2010. *The* BepiColombo mission: an outstanding tool for investigating the Hermean environment (BepiColombo Special Issue). Planet. Space Sci. 58, 40–60. https://doi.org/10.1016/j.pss.2008.06.005.
Milillo, et al., 2020. Investigating Mercury's environment with the two-spacecraft BepiColombo mission. BepiColombo Special Issue SSR 216 (5). https://doi.org/10.1007/s11214-020-00712-8.
Mura, A., Wurz, P., Lichtenegger, H.I.M., Schleicher, H., Lammer, H., Delcourt, D., Milillo, A., Orsini, S., Massetti, S., Khodachenko, M.L., 2009. The sodium exosphere of Mercury: comparison between observations during Mercury's transit and model results. Icarus 200, 1–11.
Orsini, S., Mangano, V., Milillo, A., Plainaki, C., Mura, A., Raines, J.M., De Angelis, E., Rispoli, R., Lazzarotto, F., Aronica, A., 2018. Mercury sodium exospheric emission as a proxy for solar perturbations transit. Sci. Rep. 8, 928.
Plainaki, C., Lilensten, J., Radioti, A., Andriopoulou, M., Milillo, A., Nordheim, T.A., Dandouras, I., Coustenis, A., Grassi, D., Mangano, V., Massetti, S., Orsini, S., Lucchetti, A., 2016. Planetary space weather: scientific aspects and future perspectives. J. Space Weather Space Climate 6, A31.
Potter, A.E., Morgan, T.H., 1985. Discovery of sodium in the atmosphere of Mercury. Science 229, 651–653.
Potter, A.E., Killen, R.M., Morgan, T.H., 1999. Rapid changes in the sodium exosphere of Mercury. Planet. Space Sci. 47, 1441–1448.
Potter, A.E., Killen, R.M., Sarantos, M., 2006. Spatial distribution of sodium on Mercury. Icarus 181, 1–12.
Potter, A.E., Killen, R.M., Morgan, T.H., 2007. Solar radiation acceleration effects on Mercury sodium emission. Icarus 186, 571–580.
Raines, J.M., DiBraccio, G.A., Cassidy, T.A., Delcourt, D.C., Fujimoto, M., Jia, X., Mangano, V., Milillo, A., Sarantos, M., Slavin, J.A., Wurz, P., 2015. Plasma sources in planetary magnetospheres: Mercury. Space Sci. Rev. 192, 91–144.
Schleicher, H., Wiedemann, G., Wöhl, H., Berkefeld, T., Soltau, D., 2004. Detection of neutral sodium above Mercury during the transit on 2003 May 7. A&A 425, 1119–1124.

Smyth, W.H., 1986. Nature and variability of Mercury sodium atmosphere. Nature 323, 696–699.

Solomon, S.C., McNutt Jr., R.L., Gold, R.E., Domingue, D.L., 2007. MESSENGER mission overview. Space Sci. Rev. 131, 3–39. https://doi.org/10.1007/s11214-007–9247-6.

Sprague, A.L., Kozlowski, R.W.H., Hunten, D.M., Schneider, N.M., Domingue, D.L., Wells, W.K., Schmitt, W., Fink, U., 1997. Distribution and abundance of sodium in Mercury's atmosphere, 1985–1988. Icarus 129 (2), 506–527. https://doi.org/10.1006/icar.1997.5784.